J Mater Sci (2014) 49:5676–5689
DOI 10.1007/s10853-014-8287-z

Direct synthesis of nanosized-ZSM-5/SBA-15 analog composites from preformed ZSM-5 precursors for improved catalytic performance as cracking catalyst

Xuan Hoan Vu · Ursula Bentrup · Michael Hunger · Ralph Kraehnert · Udo Armbruster · Andreas Martin

Received: 20 February 2014 / Accepted: 28 April 2014 / Published online: 14 May 2014
© Springer Science+Business Media New York 2014

Abstract Nanosized-ZSM-5/SBA-15 analog composites (ZSC) were successfully synthesized in a two-step process from zeolite seed solutions containing intact ZSM-5 nanocrystals (nano-ZSM-5) by high-temperature synthesis in mild acidic media (200 °C, pH 3.5). The ZSC solids exhibit domains of nano-ZSM-5 blended homogeneously with highly condensed, well-ordered mesoporous SBA-15 analogs containing zeolite building units. The content of nano-ZSM-5 phase and SBA-15 analog phase can be controlled by a single synthesis parameter, i.e., the pre-crystallization time of the initially formed zeolite seed solution. Compared to conventional Al-SBA-15, the acidic properties, particularly the surface density of strong Brønsted acid sites, of the ZSC are significantly improved while its micro-/mesostructures are well maintained even upon steaming at 800 °C for 24 h. The catalytic activity of the ZSC solids compared to that of commercial ZSM-5 and Al-SBA-15 samples was evaluated in the gas phase cracking of cumene and 1,3,5-tri-isopropylbenzene (TIPB) as probe reactions. The results show that the ZSC materials are effective for the conversion of both cumene and TIPB due to the increased density of the Brønsted acid sites with high accessibility provided by well-dispersed nano-ZSM-5 in the mesoporous SBA-15 analog matrix.

Electronic supplementary material The online version of this article (doi:10.1007/s10853-014-8287-z) contains supplementary material, which is available to authorized users.

X. H. Vu · U. Bentrup · U. Armbruster · A. Martin (✉)
Leibniz-Institut für Katalyse e.V. an der Universität Rostock, Albert-Einstein-Straße 29a, 18059 Rostock, Germany
e-mail: andreas.martin@catalysis.de

X. H. Vu
e-mail: hoan.vu@catalysis.de

U. Bentrup
e-mail: ursula.bentrup@catalysis.de

U. Armbruster
e-mail: udo.armbruster@catalysis.de

M. Hunger
Institute of Chemical Technology, University of Stuttgart, Pfaffenwaldring 55, 70550 Stuttgart, Germany
e-mail: michael.hunger@itc.uni-stuttgart.de

R. Kraehnert
Institut für Chemie, Technische Universität Berlin, Str. des 17. Juni 124, 10623 Berlin, Germany
e-mail: ralph.kraehnert@tu-berlin.de

Introduction

Zeolites are a class of microporous crystalline aluminosilicates that are widely used as solid acid catalysts in oil refining and petrochemical industry due to their unique properties such as strong intrinsic acidity, high hydrothermal stability, and shape selectivity [1, 2]. However, the relatively small pore size of these molecular sieves often imposes diffusion limitations especially when bulky reactant molecules are involved. The restricted access to pores and the slow diffusion transport to and from the zeolite active sites have led to lower catalyst utilization. Obviously, these properties negatively impact activity, and sometimes selectivity and/or lifetime of a zeolite-based catalyst. The principle strategies to overcome the limitations inherent in ordinary zeolites are either to reduce the diffusion path length or to develop new materials with larger pores [2].

Following the first strategy, nanosized zeolites (nanozeolites) have gained considerable interest [3, 4]. Scale-down of zeolite crystals from micrometer to nanometer

scale induces shorter diffusion path lengths and more accessible active sites through the enlargement of external surface. Clearly, this route allows taking the well-known advantages of zeolites, i.e., strong acidity and shape selectivity along with improved molecular transport characteristics, and consequently the superior catalytic performance of nano-zeolites compared to microscale zeolites as demonstrated in various reactions [5–8]. In practice, nevertheless, the application of nano-zeolites may not be feasible because of their poor stability and the difficulty in separation of nanocrystals from the reaction mixture and the significantly higher pressure drops in packed bed reactors. Therefore, nano-zeolites should be incorporated in a porous matrix wherein such crystals are dispersed and stabilized [8–10].

On the other hand, research following the latter strategy has resulted in the discovery of ordered mesoporous materials like M41S [11] or SBA-15 [12]. Such mesostructured materials with large, uniform pore sizes in the range of 2–30 nm might overcome the diffusion constraints occurring in zeolite catalysis, offering potential versatile catalysts and/or supports for conversion of bulky molecules. Unfortunately, these mesoporous materials lack the unique zeolite strong intrinsic acidity and high hydrothermal stability owing to the non-crystalline nature of mesoporous walls, which severely limits their practical uses. Accordingly, the introduction of zeolite building units into the mesoporous walls by using zeolite seeds as building block to construct a mesostructure in a two-step process has been extensively studied [13, 14]. Although the resulting ordered mesoporous materials such as MSU-S [15] or MAS-9 [16] showed greatly enhanced hydrothermal stability and acidic properties compared to conventional mesoporous aluminosilicates, these properties are still inferior to those of crystalline zeolites, thereby being not sufficient for industrial applications. The reason is that such materials do not contain the long-range atomic order characteristic of a crystalline zeolite framework. The preserved zeolite building units in the mesoporous walls envisioned to be in the range of few unit cells due to the small size of preformed zeolite nanoclusters required for the self-assembly of a mesostructure [8, 17]. Therefore, various attempts have focused on the exploration of larger zeolite seeds formed by extending the precrystallization time in the first step for the subsequent assembly of a mesostructure in the second step [17–23]. The obtained composite products consist of a zeolite phase intermixed with a mesophase in which the distribution of both phases can be controlled by the precrystallization time [18–20]. Compared to mesoporous materials with zeolite building units, the acidic properties of composites are substantially improved because of the zeolite phase present. However, these syntheses were carried out in mild temperatures (typically 100–150 °C), resulting in the imperfectly condensed mesoporous phase, thus the unsatisfactory hydrothermal stability. Furthermore, the growth of zeolite precursors to micro-sized zeolite crystals, in some cases, may not be controllable in a basic media [18, 22, 23]. Recently, we developed an effective method for further improving the hydrothermal stability and acidic properties of ordered mesoporous SBA-15 analogs assembled from ZSM-5 precursors (SAZ) by high-temperature synthesis and pH adjustment [24]. The ordered mesostructure of the resulting SAZ solids is well preserved even upon steaming at 800 °C for 4 h, while their acidic properties are significantly enhanced in terms of both the number of acidic sites and their strength. Like other known SBA-15 analogs, however, the acidic nature of the SAZ solids is still much weaker than those of conventional ZSM-5.

In this study, we extend this method by employing the precursor solution containing intact nano-ZSM-5 crystals for the direct synthesis of composite materials in order to improve the acidic properties, particularly zeolite Brønsted acidity. The rationale behind this idea is to use highly condensed, ordered mesoporous SBA-15 analogs with zeolite building units developed in our previous work as an advanced matrix for the dispersion of nano-ZSM-5. By this way, the advantages of nano-ZSM-5 and those of SBA-15 analogs can be combined to create superior materials. To achieve this, the seed solution is pre-crystallized for a longer time period to partially form well-defined ZSM-5 nanocrystals before being used for subsequent self-assembly of a mesostructure via high-temperature synthesis and pH adjustment. After the systematic characterization of physicochemical aspects, the catalytic performances of the prepared composites are ultimately evaluated in the gas phase cracking of cumene and 1,3,5-tri-isopropylbenzene (TIPB) as probe reactions to visualize the benefits of increased Brønsted acidity whose access is enhanced by the bimodal pore system.

Experimental details

Chemicals

The chemicals used for synthesis were tetraethyl orthosilicate (TEOS, 99 %, Aldrich), tetrapropylammonium hydroxide (TPAOH, 20 % in water, Aldrich), aluminum isopropoxide (AIP, 98 %, Aldrich), triblock copolymer pluronic P123 (EO20PO70EO20, $M_W = 5800$ g/mole, Aldrich), hydrochloric acid (HCl, 37 % in water, J.T. Baker), ammonium hydroxide (25 % of NH_3 in water, Acros), Cumene (98 %, Aldrich), and 1,3,5-tri-isopropyl benzene (TIPB, 96 %, Aldrich). All reagents were used as received without further purification.

Synthesis of composites

The synthesis procedure consists of two major steps. In a first step, seed solutions are synthesized and pre-crystallized for different time periods. A second step of hydrothermal treatment in the presence of a supramolecular template converts the fraction of precursors that has not been consumed in the first step into an ordered mesoporous aluminosilicate that surrounds and disperses the initial zeolite crystals. The content of microporous and mesoporous phase can be controlled by controlling the precursor growth to zeolite crystals in the first step.

A typical synthesis is described as follows: 6.0 g of TEOS, 10.0 g of TPAOH, 2.0 g of distilled H_2O, and 0.19 g of AIP were mixed at room temperature and stirred overnight to complete the hydrolysis, followed by pre-crystallization at 90 °C for various time periods (6, 12, 24, and 36 h) in a reflux system to obtain the desired precursor solutions with the final molar composition of 60 SiO_2: Al_2O_3: 20 TPAOH: 1200 H_2O: 240 EtOH. Simultaneously, the P123 solution was prepared by dissolving 2.0 g of P123 in 75 mL of 1.6 M HCl at room temperature and stirring for 4 h to form the clear solution. Then, the ZSM-5 precursor solution prepared as described above was added drop wise to the P123 solution, followed by aging at 40 °C for 24 h. Before transferring the mixture into a Teflon-lined autoclave for more incorporated aluminum and further silica condensation at 200 °C for 24 h, the pH value was adjusted to 3.5 with aqueous NH_3 solution. The final product was filtered off, washed with distilled water, and dried at 100 °C for 12 h. The as-synthesized material was calcined in air at 550 °C for 5 h with a heating rate of 2 K/min to remove the organic template. The calcined solid was transformed into the protonated form by two consecutive exchanges in 0.5 M NH_4NO_3 solution at 80 °C for 4 h. The obtained catalysts are denoted as ZSC-x, where ZSC represents the nanosized-ZSM-5/SBA-15 analog composite, and x is the duration of precrystallization in the first step.

For the purpose of comparison, Al-SBA-15 was prepared under the same condition as for synthesis of ZSC samples, but using conventional silica-based precursors instead of zeolite seeds. In addition, commercial Al-rich submicroscale H-ZSM-5 (Zeocat PZ-2/25, ZeoChem AG) was used to provide a benchmark.

Physico-chemical characterization

Small/wide angle X-ray scattering (SAXS/WAXS) measurements were carried out using a Kratky-type instrument (SAXSess, Anton Paar, Austria) operated at 40 kV and 50 mA in slit collimation using a two-dimensional CCD detector and an imaging plate (Kodak X-ray film), respectively. The 2D scattering pattern was converted into a one-dimensional scattering curve as a function of the magnitude of the scattering vector $q = (4\pi/\lambda) \times \sin(\theta/2)$ with SAXSQuant Software (Anton Paar). A Göbel mirror was used to convert the divergent polychromatic X-ray beam into a collimated line-shaped beam of Cu K_α radiation ($\lambda = 0.154$ nm). Slit collimation of the primary beam was applied in order to increase the flux and to improve the signal quality. The sample cell consisted of a metal body with two windows for the X-ray beam. The powdered samples were placed between two layers of Scotch® tape. Scattering profiles of the mesoporous materials were obtained by subtraction of the detector current background and the scattering pattern of the Scotch® tape from the experimental scattering patterns. Correction of instrumental broadening effects (smearing) was carried out with SAXSQuant software using the slit length profile determined in a separate experiment.

X-ray diffraction (XRD) measurements were carried out on a θ/θ diffractometer (X'Pert Pro from Panalytical, Almelo, Netherlands) with Cu K_α radiation ($\lambda = 0.15418$ nm; 40 kV, 40 mA) and an X'Celerator RTMS Detector. The alignment was checked by use of a silicon standard.

The Fourier transform infrared spectroscopy (FT-IR) spectra were recorded on an ALPHA-FT-IR spectrometer (Bruker) using the attenuated total reflection (ATR) sampling technique.

Scanning electron microscope (SEM) imaging was performed using a field emission SEM JEOL 7401F operated at an acceleration voltage of 4 kV and a working distance of 4 mm. For the imaging, powder samples were attached to carbon tape.

Transmission electron microscopy (TEM) measurements were performed at 200 kV with a JEM-ARM200F (JEOL), which is aberration-corrected by a CESCOR (CEOS) for the scanning transmission microscopic (STEM) applications. The sample was placed on a holey carbon supported Cu-grid (mesh 300) as received and transferred to the microscope.

The solid-state NMR investigations were performed with the hydrated material using a Bruker BioSpin Avance III 400WB spectrometer at the resonance frequencies of 104.3 and 79.5 MHz for ^{27}Al and ^{29}Si nuclei, respectively. The MAS NMR spectra were recorded upon single pulse excitation of $\pi/6$ for ^{27}Al and $\pi/2$ for ^{29}Si nuclei, with repetition times of 0.5 and 30 s, respectively, and high-power proton decoupling (HPDEC) in the case of studying ^{29}Si nuclei. The sample spinning rates were 8 and 4 kHz for the investigation of ^{27}Al and ^{29}Si nuclei, respectively.

Nitrogen physisorption measurements were carried out at −196 °C with an ASAP 2010 apparatus (Micromeritics). Before measurements, the samples were degassed at 180 °C in vacuum for 10 h. The specific BET surface area was calculated using adsorption data at a relative pressure

(p/p_0) of 0.05–0.25, and the total pore volume was estimated from the amount adsorbed at a relative pressure of about 0.976. The pore size distributions were obtained from the desorption branch of the isotherm using the corrected form of the Kelvin equation by means of the Barrett–Joyner–Halenda method with a cylindrical pore model.

Temperature-programmed desorption of ammonia (NH_3-TPD) measurements were carried out in a quartz tube reactor in the range of 100–550 °C with the desorbed ammonia being continuously detected by a thermal conductivity detector (TCD, Gow-Mac Instruments Co.). The samples were first activated at 550 °C for 0.5 h under helium flow. After the reactor was cooled to 100 °C, the samples were swept with ammonia for 0.5 h for adsorption. Then, the feed gas was switched to helium to remove the physically adsorbed ammonia molecules until the TCD baseline was flat. After that, the temperature was increased to 550 °C with a heating rate of 10 K/min, and desorbed ammonia was quantitatively analyzed by the external standard method using the integrated desorption peak area compared to the standard curve.

The FT-IR measurements for the acidity investigations were performed on a Tensor 27 spectrometer (Bruker) using self-supporting wafers and pyridine as probe molecule. A homemade, heatable reaction cell with CaF_2 windows connected to a gas-dosing and evacuation system was used. The sample powders were pressed into self-supporting discs with a diameter of 20 mm and a weight of 50 mg. Before pyridine adsorption, the samples were pretreated by heating in flowing He up to 400 °C and holding this temperature for 10 min. Then, the samples were cooled in the respective gas stream to room temperature. Pyridine was adsorbed by bubbling the He flow through a pyridine-containing saturator until saturation, followed by evacuation of the reaction cell to remove physisorbed pyridine. Desorption of pyridine was studied by heating the sample under He stream with 5 K/min up to 400 °C. Spectra were recorded at different temperatures with 2 cm^{-1} resolution and 100 scans.

The Al and Si contents of the calcined samples were determined by ICP-AES (715-ES, Varian) and AAS (Analyst 300, Perkin Elmer), respectively. For this purpose, the samples were digested with a mixture of HCl–HNO_3–HF in order to dissolve them completely.

Hydrothermal stability tests

The hydrothermal stability of the representative sample ZSC-24 was evaluated by steaming at 800 °C with 30 % water vapor in helium flow (30 mL/min) for 24 h. The sample was sieved and 0.2 g with a particle size between 300 and 700 μm was loaded into a quartz tube reactor. The sample was heated to 800 °C under helium flow with a rate of 20 K/min. As soon as the temperature reached 800 °C, the helium flow containing 30 % steam was introduced into the tube reactor. The steam treatment time was 24 h. After the steam treatment, the sample was cooled down and characterized by XRD, SAXS, and nitrogen physisorption to re-evaluate the structural and textural properties.

Catalytic experiments

The gas phase cracking of cumene and 1,3,5-triisopropyl benzene (TIPB) was carried out in a fixed-bed down-flow stainless steel reactor (10 mm internal diameter) equipped with mass flow controllers for reactant metering. Typically, a fixed amount of the sieved catalyst (0.4 g for cumene cracking or 0.6 g for TIPB cracking, particle size 300–700 μm, diluted with 2.0 g of quartz beads of the same size) was placed in the reactor. Prior to the reaction, the sample was activated in N_2 flow at 300 °C for 2 h to remove physically adsorbed water. The liquid reactant (cumene or TIPB) was fed at a rate of 0.6 g/h by a liquid mass flow controller (Liqui-Flow, Bronkhorst) coupled to a Controlled Evaporator Mixer (CEM, Bronkhorst), using N_2 flow (90 mL/min) as a carrier gas. By this way, the reactant was mixed with N_2 and then evaporated before entering the reactor. The catalytic cracking was conducted at 300 °C under atmospheric pressure. Feed and product samples were analyzed with an online gas chromatograph (HP 5890, equipped with a sampling valve, a fused silica capillary column (HP5, 50 m × 0.32 mm × 0.52 μm) and a flame ionization detector. The temperature of the column was held at 50 °C for 2 min, then increased to 280 °C at a rate of 15 K/min and held for 4 min.

Results and discussion

Evolution of precursors to zeolite crystals

Understanding of evolution of precursors to zeolite crystals during the precrystallization process is of fundamental importance for the preparation of novel hierarchical materials from preformed zeolite precursors. In this study, the ZSM-5 seed solution was preheated at 90 °C in a reflux system for different time periods and the evolution of precursor nanoclusters to zeolite crystals was monitored by WAXS (Fig. 1).

As can be seen from Fig. 1, within short precrystallization periods (6 and 12 h) crystalline ZSM-5 nanoparticles do not form, as confirmed by the absence of reflections in the WAXS patterns. Extending the reaction time to 24 h, the first indications of ZSM-5 crystals appear with the small typical reflections of MFI topology at $2\theta = 8.0°$, 8.8°, and 23.1°. This indicates that the formation of ZSM-5

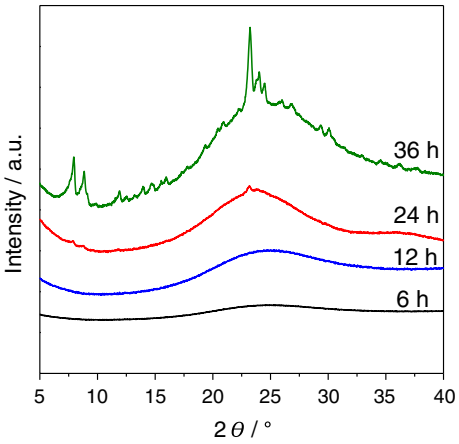


Fig. 1 WAXS patterns of the ZSM-5 precursor solution after precrystallization for 6, 12, 24, and 36 h

nanocrystals proceeds progressively with the precrystallization time, leading to an adequate crystalline phase that can be detected by WAXS [25]. These MFI reflections look well-developed upon aging for 36 h, suggesting a dominant fraction of formed ZSM-5 nanocrystals. Thus, the formation and content of crystalline ZSM-5 phase in the seed solution can be controlled by controlling the precrystallization time. These findings offer possibilities for tuning the content of ZSM-5 nanocrystals with respect to the mesoporous matrix that can be directly developed from unreacted precursors in a subsequent step [18–20].

Structural and textural characterization

Figure 2 shows SAXS (a) and XRD (b) patterns of ZSC samples prepared from preformed ZSM-5 precursors with different aging time periods. As shown in Fig. 2a, ZSC-6, ZSC-12, and ZSC-24, synthesized from the seed solutions pre-crystallized for 6, 12, and 24 h, respectively, exhibit three well-resolved reflections indexed as the 100, 110, and 200 reflections of 2D hexagonal (p6 mm) symmetry, indicative of a highly ordered mesostructure (SBA-15 analogs). After a more extended precrystallization of 36 h (ZSC-36), no such reflections can be observed, suggesting the absence of an ordered mesostructure in this sample. Wide-angle XRD patterns (Fig. 2b) yield complementary information on the presence of a crystalline ZSM-5 phase in the samples ZSC-24 and ZSC-36. Both samples show clear reflections in the 2θ regions of 8–10° and 23–25°, indicative of ZSM-5 crystals. In contrast, no such reflections were detected in the samples ZSC-6 and ZSC-12, implying a very low content or absence of a crystalline zeolite structure. The reflections become sharper and more prominent with increasing the precrystallization time, suggesting a higher crystallinity in ZSC-36 compared to ZSC-24.

The complementary SAXS and XRD data can be interpreted as a gradual transition between a mesoporous SBA-15 type phase and a microporous ZSM-5 phase that is controlled by the precrystallization time applied in the ZSM-5 precursor synthesis. Controlled formation of composite materials is then a question of kinetic control of the synthesis process. For the longest precrystallization time (36 h), the zeolite crystal growth consumes all precursor species; hence the mesoporous framework phase cannot be formed anymore. In contrast, for shorter precrystallization times (ZSC-6 and ZSC-12), the precursors have been hardly consumed in the zeolite formation; hence the mesoporous frame can be formed around the zeolite domains in the second synthesis step. Thus, ZSC-24 contains sufficient amounts of ordered mesoporous SBA-15 analogs (Fig. 2a) and crystalline ZSM-5 (Fig. 2b), in order to form detectable amounts of ordered mesoporous phase and microporous zeolite phase. This interpretation is also in agreement with the literature, where precursor species that have not reacted to form zeolite crystals could be used as building units for self-assembly of a mesostructure [18–20].

FT-IR spectroscopy supports the outlined hypothesis. From Fig. 2c, it can be seen that ZSC-36 displays a sharp band at ca. 548 cm^{-1}, which is assigned to asymmetric stretching mode of pentasil units in the MFI zeolite topology, confirming the relatively high ZSM-5 crystallinity [21]. The spectrum of ZSC-24 shows the same absorption band, but less pronounced, suggesting that this sample is less crystallized. In case of ZSC-6 and ZSC-12, only a very small band at ca. 548 cm^{-1} can be observed. It is likely that the atomic order of ZSC-6 and ZSC-12 is only in the range of a few unit cells that is not adequate to be detected by XRD (Fig. 2b), being consistent with the reports by Liu et al. [15] and Han et al. [16].

Also, SEM and TEM analyses support the interpretation of a precrystallization time controlled tuning of microporous and mesoporous phase content. Figure 3 displays SEM micrographs of ZSC materials synthesized with different precrystallization time periods of the ZSM-5 solution of 6 h (ZSC-6, Fig. 3a, e), 12 h (ZSC-12, Fig. 3b, f), 24 h (ZSC-24, Fig. 3c, g) and 36 h (ZSC-36, Fig. 3d, h). For each material, the SEM images at magnifications of 20× (a–d) as well as 100× (e–h) are shown along with FFT (Fast Fourier Transform) transformations of the 100× images to analyze the presence of ordered mesoporosity (insets in Fig. 3e–h). The images for all samples indicate the presence of two different intermixed phases with clearly distinct particle sizes and particle morphology. The content of both phases clearly shifts with increasing the precrystallization time. ZSC-6, the material with the shortest precrystallization time of the ZSM-5 seed solution shows the predominant presence of particles of about 300–600 nm diameter and of very small amounts of an

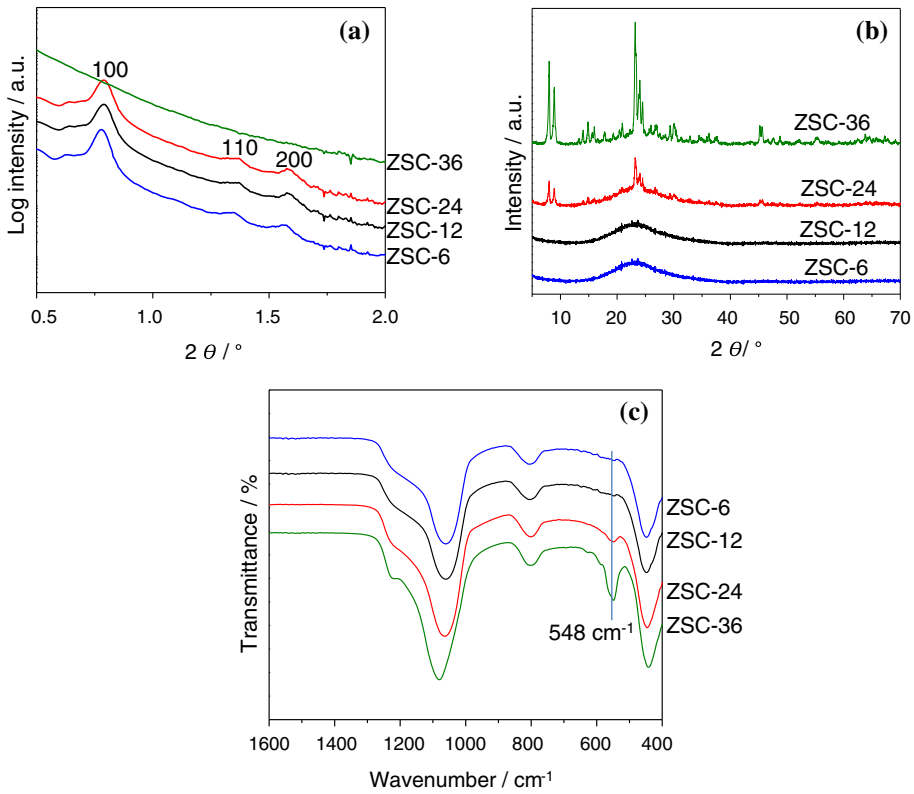


Fig. 2 SAXS (**a**) and XRD (**b**) patterns and FT-IR spectra (**c**) of ZSC composites

additional phase of about 50–100 nm particle size (Fig. 3a). The entire larger particles feature a distinct type of mesoporosity with parallel channels (Fig. 3e), a structure typical for SBA-15 type materials. The ordered pore arrangement is confirmed by FFT analysis of the corresponding SEM image (inset in Fig. 3e), which shows two symmetric spots that correspond well with the typical hexagonal pore arrangement. The two types of particle domains can therefore be assigned to a mesoporous phase (larger particles) and microporous zeolite phase (smaller particles). Both types of phases are observed also in the samples synthesized with the longer precrystallization times of 12 h (Fig. 3b, f), 24 h (Fig. 3c, g) and 36 h (Fig. 3d, h). However, with increasing the precrystallization time, the content of the mesoporous phase decreases gradually, whereas a higher content of the ZSM-5 phase is apparent (from Fig. 3b, c, d). Preserved mesoporosity is confirmed by higher resolution SEM images and corresponding FFT images for 12 h (Fig. 3f) and 24 h (Fig. 3g) precrystallization time, whereas the sample pre-crystallized for 36 h retains hardly any mesoporous phase (Fig. 3d, h, note the absence of spots in the FFT inset). Hence, the relative content of the mesoporous phase and microporous zeolite phase can be easily adjusted synthetically by increasing the precrystallization time of the ZSM-5 precursor solution. These findings are in line with the earlier works [18–20]; however, in our study, the nano-ZSM-5 domains are smaller and more uniforms achieved by a careful synthesis of the zeolite seed solution.

The SEM images of the reference samples are presented in Fig. S1 (Supplementary material). From Fig. S1a, the ordered mesostructure of Al-SBA-15 can be clearly seen, while Fig. S1b reveals that H-ZSM-5 consists of small crystals (ca. 250 nm) and their aggregates (ca. 800 nm).

TEM analysis validates the phase assignments of a mesoporous phase and a microporous crystalline ZSM-5 phase. The TEM images of ZSC-24 (Fig. 4) indicate that this material consists of an ordered hexagonal mesoporous structure (pore channels clearly evident in Fig. 4a) coexisting with fairly uniform ZSM-5 nanoparticles (note the black domains), leading to a composite with well-dispersed nano-ZSM-5 crystals. The lattice fringe of a nano-ZSM-5 domain embedded in the mesoporous matrix can be visualized through the TEM image with high magnification (Fig. 4b). Parts of the ZSM-5 crystals are therefore in close contact with the mesoporous phase. Such close contact between ZSM-5 phase and mesoporous phase has proven to form a highly interconnected pore structure, which greatly benefits the catalytic performance compared to the mechanical mixture of the corresponding zeolites and mesoporous materials [8, 9, 26, 27].

The local environment of the Al and Si atoms in the representative sample ZSC-24 was investigated by ^{27}Al and ^{29}Si MAS NMR spectroscopy, respectively (Fig. 5).

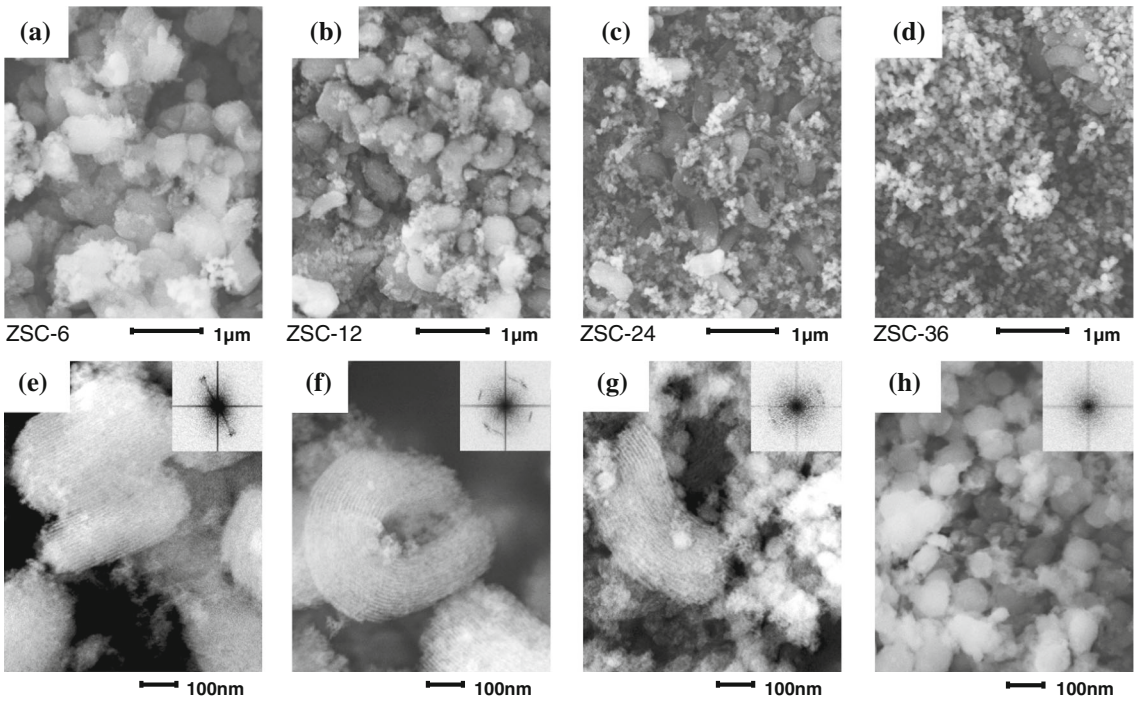


Fig. 3 SEM images of ZSC composites with the various precrystallization times of 6, 12, 24, or 36 h (from left to right). SEM images with 20× magnification are shown in upper row (**a**–**d**) and images with 100× in lower row (**e**–**h**). *Insets* show FFT images of the respective SEMs

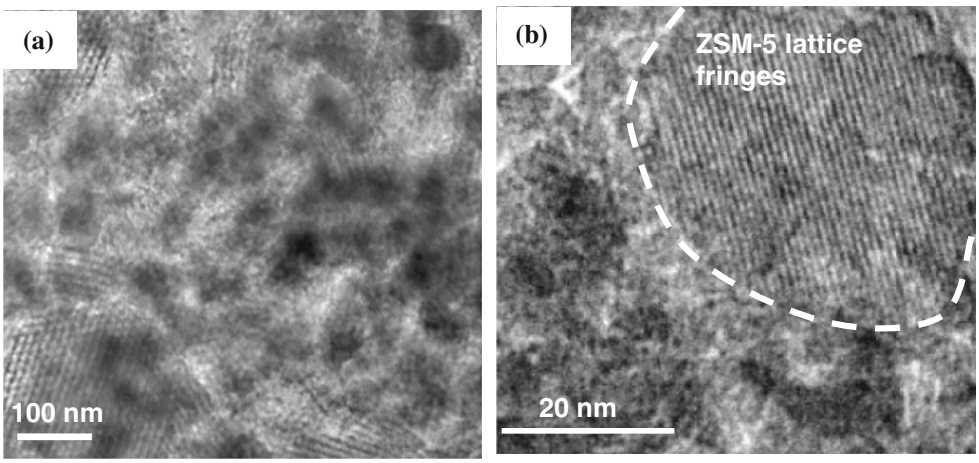


Fig. 4 TEM images of ZSC-24: **a** low magnification and **b** high magnification

The ^{27}Al MAS NMR spectrum (Fig. 5a) shows a dominant signal centered at approximately 53 ppm and a much weaker signal at ca. 0 ppm, which are attributed to tetrahedrally and octahedrally coordinated aluminum, respectively. This indicates that most of the aluminum is incorporated into the material framework [28]. From Fig. 5b, it can be seen that the ^{29}Si MAS NMR spectrum displays a dominating signal at −112 ppm due to Q4 silicon species (Si(4Si)) and a broad, low-field shoulder at −95 to −105 ppm. This shift range is typical for Q2 and Q3 silicon species (Si(2Si,2OH) and Si(3Si,1OH), respectively), but also for silicon atoms with an oxygen bridge to tetrahedrally coordinated framework aluminum species (Si(3Si,1Al)). The latter silicon species are responsible for the formation of Brønsted acid sites, e.g., in zeolite ZSM-5 [28].

In general, the ^{29}Si MAS NMR spectrum indicates a high degree of silicon condensation in this sample. These data clearly demonstrate the advantages of high-temperature synthesis for the preparation of composite materials with respect to the mild temperature synthesis whose products such as MSU-S_{BETA}/zeolite beta [18] or MCM-14/zeolite beta [29] suffered from large fractions of octahedral Al and much less condensed mesoporous walls.

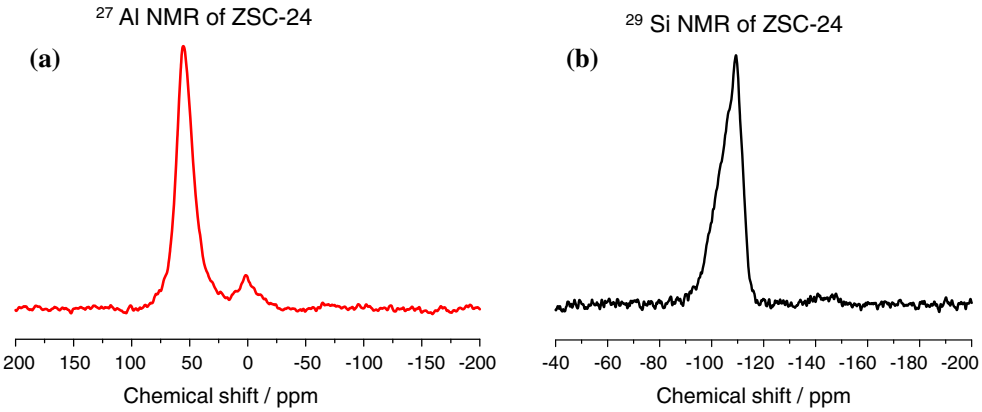


Fig. 5 ^{27}Al (**a**) and ^{29}Si (**b**) MAS NMR spectra of ZSC-24

The N_2 adsorption/desorption isotherms and corresponding pore size distributions of ZSC composites are illustrated in Fig. 6. The samples ZSC-6, ZSC-12, and ZSC-24 exhibit type IV isotherms with a very steep capillary condensation step in the relative pressure (p/p_0) range of 0.7–0.9, which is characteristic for an ordered mesostructure with a large and uniform pore size. It should be noted that the isotherm of ZSC-24 shows a relatively steep increase of the adsorbed N_2 amount at low relative pressures ($p/p_0 < 0.01$), indicating the presence of micropores in this sample. The same phenomenon is observed from the isotherm of ZSC-36, but more obvious, which clearly confirms its microporous nature. In addition, a high relative pressure uptake ($p/p_0 > 0.9$) can be seen for all samples, indicative of inter-crystalline pores. These results can be directly reflected by the pore size distribution as shown in Fig. 6b. The first three samples have narrow pore size distribution curves centered at approximately 9.0 nm (ZSC-6, ZSC-12) and 7.5 nm (ZSC-24). In contrast, the pore size distribution of ZSC-36 is broader, implying that this sample contains only interparticle voids. The detailed information about the textural properties of ZSC materials as well reference samples is summarized in Table 1. The specific BET surface area of all samples lies in the range of 324–466 m^2/g, which represents that of both highly condensed mesoporous materials and microporous zeolites [6, 30]. However, the total pore volume decreases sharply with increasing the zeolite phase content, from 0.97–0.84 cm^3/g (ZSC-6, ZSC-12, ZSC-24, and Al-SBA-15) to 0.27–0.21 cm^3/g (ZSC-36 and H-ZSM-5). This is possibly due to the lack of a well-defined mesoporous phase in the last two samples. Notably, ZSC-24 exhibits a relatively thicker pore wall (5.4 nm) than ZSC-6 and ZSC-12 (3.8 and 4.0 nm, respectively). It is likely that the longer aging time in the first step has led to a precursor solution with larger nanoseeds. Therefore, the use of these larger nanoseeds as building units to construct the mesostructure has led to a thicker pore wall of the resulting material.

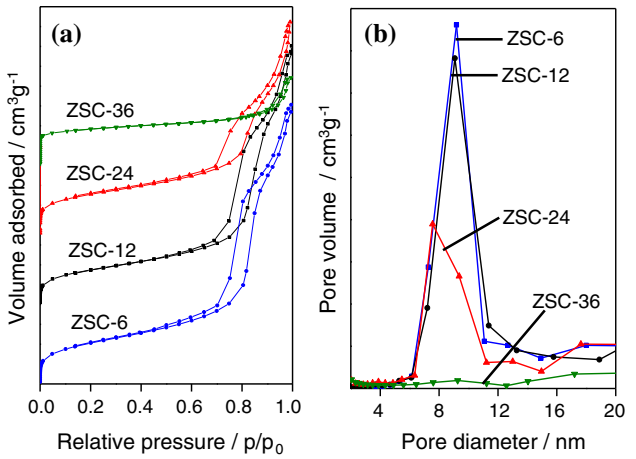


Fig. 6 N_2 sorption isotherms (**a**) and the corresponding pore size distribution curves (**b**) of ZSC composites

Table 1 Structural and textural properties of ZSC composites, Al-SBA-15, and H-ZSM-5

Sample	d_{100} (nm)	a_0 (nm)	D_p (nm)	W (nm)	S_{BET} (m^2/g)	V_t (cm^3/g)
ZSC-6	11.2	12.9	9.1	3.8	412	0.97
ZSC-12	11.3	13.0	9.0	4.0	346	0.98
ZSC-24	11.2	12.9	7.5	5.4	361	0.84
ZSC-36	–	–	–	–	324	0.27
Al-SBA-15[a]	10.2	11.7	7.2	4.5	466	0.93
H-ZSM-5[b]	–	–	–	–	373	0.21

a_0 unit cell parameter ($a_0 = 2 \times d_{100}/3^{1/2}$), D_p pore diameter, W pore wall thickness ($W = a_0 - D_p$), V_t total pore volume; the missing parameters of ZSC-36 are due to the absence of an ordered mesostructure

[a] Synthesized by the same procedure as ZSC, but using the conventional silica-based source instead of zeolite seeds

[b] Commercial Al-rich H-ZSM-5 (Zeocat PZ-2/25)

Acidity study

The acidic properties (number of sites and their strength) of ZSC composites and the reference materials H-ZSM-5 and Al-SBA-15 were determined by NH_3-TPD. The results are presented in Fig. 7 and Table 2. In general, all ZSC samples exhibit a similar TPD profile with two desorption peaks. The dominant peak around 200 °C can be attributed to weak acid sites, whereas the second broader peak like a tail in the range of 300–500 °C shows the presence of medium and strong acid sites. The second desorption peak of ZSC-36 appears more pronounced in comparison to that of the other samples suggesting a higher fraction of strong acid sites in ZSC-36.

From Table 2, it can be seen that extending the precrystallization time slightly increases both the total acidity (i.e., number of sites) and the incorporated Al content in the final products. This might be explained by a larger content of zeolite phase generated by a longer precrystallization time period. The total acidity of ZSC-24 and ZSC-36 is noticeably higher than that of ZSC-6 and ZSC-12, which may reflect the sufficient amount of nano-ZSM-5 phase that can be detected by XRD (Fig. 2b). It is also noteworthy that the number of acid sites is lower for ZSC-36 than for ZSC-24 although the former contains mostly nano-ZSM-5 domains as confirmed by the data of SAXS and XRD (Fig. 2a, b). The possible explanation was pointed out by Waller et al. [8] who found that the interaction at the interface of microporous and mesoporous phases caused an increased number of acid sites in the resulting composite. Compared to commercial Al-rich H-ZSM-5, ZSC materials have significantly lower acidity in terms of both the number of acidic sites and their acid strength, but definitely increased acidity compared to those of Al-SBA-15 prepared from conventional silica precursors (Fig. 7b, Table 2). The improved acidity of these ZSC samples may result from the presence of nano-ZSM-5 and the retention of zeolite building units in SBA-15 analog phase [13, 15]. However, NH_3-TPD can only uncover strength and number of acid sites but one cannot distinguish different types of acid sites. Therefore, FT-IR spectroscopy of adsorbed pyridine was carried out over the ZSC and reference samples in order to determine and discriminate the contribution of Brønsted and Lewis acid sites.

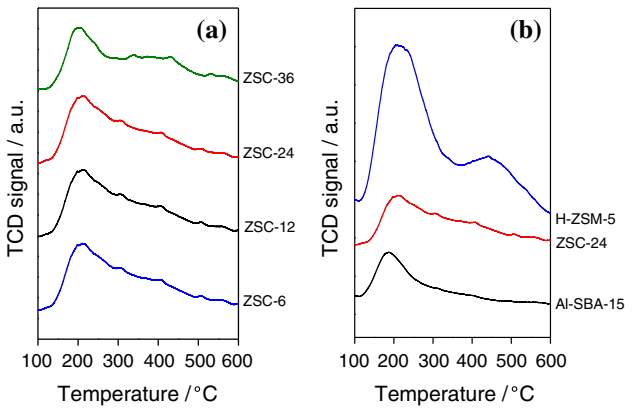


Fig. 7 NH_3-TPD profiles of (**a**) ZSC composites and (**b**) ZSC-24 with respect to Al-SBA-15 and H-ZSM-5

Table 2 Acidity of ZSC composites, Al-SBA-15, and H-ZSM-5

Sample	Si/Al ratio in gel	Si/Al ratio in products[c]	Total acidity (mmol NH_3/g)
ZSC-6	30	34	0.26
ZSC-12	30	32	0.27
ZSC-24	30	30	0.34
ZSC-36	30	27	0.31
Al-SBA-15[a]	30	45	0.18
H-ZSM-5[b]	n.a.	11	1.24

[a] Synthesized by the same procedure as ZSC, but using the conventional silica based source instead of zeolite seeds

[b] Commercial Al-rich H-ZSM-5 (Zeocat PZ-2/25)

[c] Si, Al content in the products analyzed by AAS and ICP, respectively

Figure 8 shows FT-IR spectra of pyridine adsorbed on the surface of the representative ZSC samples: ZSC-12, ZSC-24, and ZSC-36 after adsorption procedure and evacuation at 200, 300, and 400 °C. Those of the reference samples are depicted in Fig. S2 (Supplementary material). In general, FT-IR spectra of pyridine adsorbed on these samples display clearly two typical bands. A band at approximately 1542 cm^{-1} can be attributed to the pyridinium cation on Brønsted acid sites (PyH^+, BS), while a band at ca. 1450 cm^{-1} is characteristic of pyridine coordinatively bound to a Lewis acid site (PyL, LS). The quantitative estimation of BS and LS was obtained by normalizing the integral intensity of the corresponding bands to the BET surface area (Table 3). As expected, the density of BS in Al-SBA-15 is relatively low and significantly reduces with desorption temperature, suggesting dominant weak BS. In contrast, ZSC-36 dominated by nano-ZSM-5 domains undergoes the least decrease after evacuation at 400 °C, resulting in the highest concentration of pyridine adsorbed on BS compared to the other ZSC composites. Therefore, this desorption temperature is taken as borderline with the assumption that weak and medium BS release pyridine while strong BS still retain it after evacuation at 400 °C. Clearly, the higher content of zeolite phase, the larger concentration of strong BS: H-ZSM-5 > ZSC-36 > ZSC-24 > ZSC-12 (ZSC-6) > Al-SBA-15. A larger strong BS density for ZSC composites than for

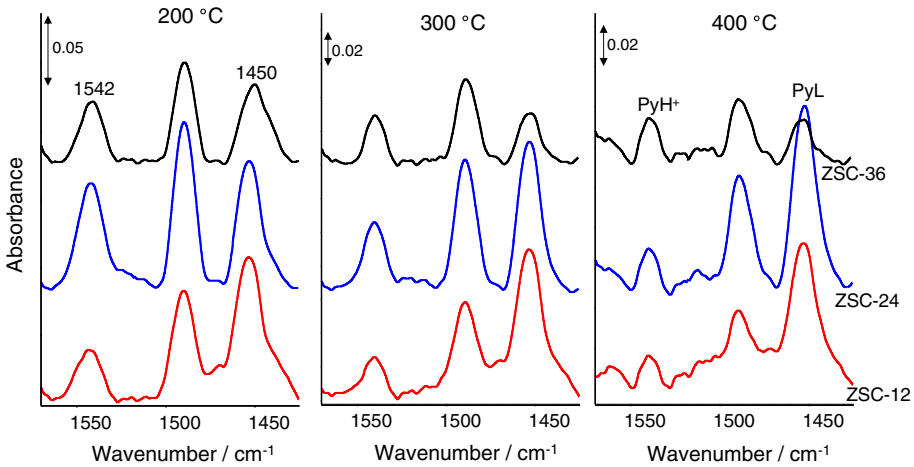


Fig. 8 FT-IR spectra of adsorbed pyridine on the representative ZSC composites: ZSC-12, ZSC-24, and ZSC-36 after evacuation at 200, 300, and 400 °C

Table 3 Normalized integral FT-IR band intensities of adsorbed pyridine over ZSC composites upon evacuation at 200, 300, and 400 °C

Sample	200 °C			300 °C			400 °C		
	B	*L*	*B*/*L*	*B*	*L*	*B*/*L*	*B*	*L*	*B*/*L*
ZSC-12	1.79	3.79	0.47	0.95	3.09	0.30	0.49	2.66	0.18
ZSC-24	3.02	3.68	0.82	1.39	3.55	0.39	0.66	3.52	0.19
ZSC-36	2.10	3.02	0.69	1.14	1.42	0.80	0.80	1.02	0.78
Al-SBA-15[a]	1.58	2.21	0.71	0.92	1.97	0.46	0.30	1.88	0.16
H-ZSM-5[b]	11.44	4.20	2.73	8.81	2.90	3.03	5.73	2.25	2.47

The data of H-ZSM-5 and Al-SBA-15 are included for reference. *B*, *L* are the integral band intensities of pyridine adsorbed on BS (1542 cm^{-1}) and LS (1450 cm^{-1}) normalized to the BET surface areas, respectively ($\times 10^{-3}$, a.u.)

[a] Synthesized by the same procedure as ZSC, but using the conventional silica-based source instead of zeolite seeds

[b] Commercial submicroscale Al-rich H-ZSM-5 (Zeocat PZ-2/25)

Al-SBA-15 can be assigned to the retention of zeolite building units coupled to the presence of nano-ZSM-5 domains. However, compared to commercial Al-rich H-ZSM-5, the strong BS density of ZSC composites is still considerably lower owing to the smaller content of zeolite phase. Regarding LS, the opposite can be observed. Both Al-SBA-15 and ZSC samples possess high concentrations of strong LS. However, it is worth noting that the LS density is always relatively lower for ZSC-36 among the other samples, possibly because of almost complete absence of mesoporous phase. Thus, the concentration of BS, in particular strong BS increases with the zeolite phase increase whereas that of strong LS depends heavily on the mesoporous phase.

It is well-known that strong BS are typical for zeolites with bridging hydroxyl groups (Si–OH–Al) originated from tetrahedral Al in the zeolite framework. The nature of LS is not clear, but strong LS are mostly formed by partial extraction of Al framework, identified as octahedral Al. As a result, zeolites like H-ZSM-5 are usually dominated by strong BS [31, 32]. On the other hand, most incorporated Al in amorphous mesoporous materials like Al-SBA-15 appears to contribute to LS acidity regardless of tetrahedral or octahedral Al due to lack of a long-range atomic order [33]. Several strong BS can be also generated by the interaction of silanol groups with tetrahedral Al nearby [34]. Generally speaking, the acidic properties of amorphous mesoporous materials are characterized by strong LS and weak BS [32, 33]. Using zeolite nanoseeds as building blocks to construct a mesostructure has been known as an effective way to improve strong BS due to the retention of zeolite building units in the mesoporous walls [13]. Hence, the increase in strong BS of ZSC composites compared to Al-SBA-15 might arise from the presence of nano-ZSM-5 phase as well as the preservation of zeolite building units in the mesoporous phase. However, the higher density of strong BS for ZSC-24 and ZSC-36 further stresses the importance of nano-ZSM-5 phase present when the aim is to enhance strong BS with improved accessibility [8–10]. Furthermore, it is interesting to see that the contribution of BS and LS in the ZSC composites can be tuned for different reactions by controlling the distribution of microporous and mesoporous phases via the precrystallization time.

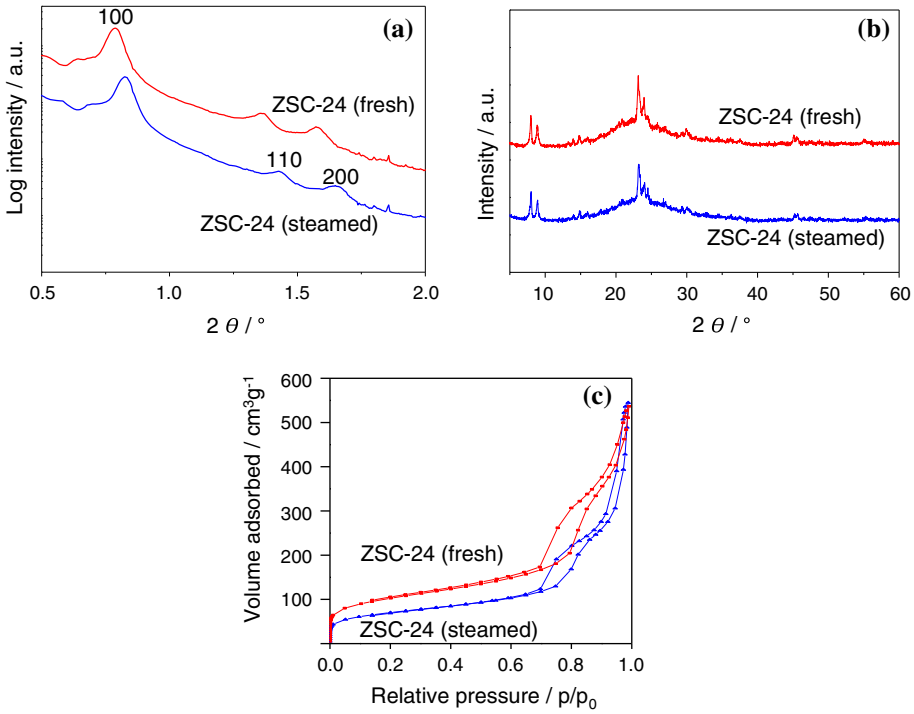


Fig. 9 Effect of steaming of catalyst ZSC-24 for 24 h at 800 °C: **a** SAXS, **b** XRD, and **c** N_2 sorption isotherms

Hydrothermal stability

As above-mentioned, hydrothermal stability is of crucial importance when potential catalysts are targeted for the fluid catalytic cracking (FCC) process. This is because in the FCC process, the catalyst has to expose to severe conditions, i.e., 700–800 °C in the presence of steam during regeneration step [35, 36]. Therefore, the hydrothermal stability was evaluated by treatment of the representative sample ZSC-24 ($T = 800$ °C, 30 % steam in He flow (30 mL/min)) and subsequent SAXS, XRD, and N_2 sorption analyses. The results are shown in Fig. 9a (SAXS), b (XRD), and c (N_2 sorption).

Upon steaming even for 24 h, ZSC-24 still exhibits three well-resolved reflections in the SAXS pattern assigned to the 100, 110, and 200 planes of highly ordered hexagonal symmetry, confirming the good preservation of its ordered mesostructure (Fig. 9a). Similarly, in the wide-angle range, the XRD patterns of the untreated and treated sample (Fig. 9b) show almost identical reflections, typical of MFI topology and indicative of the excellent preservation of ZSM-5 nanocrystals. The high stability of ZSC-24 against steaming is finally assured by N_2 adsorption and desorption measurements (Fig. 9c). Only little change can be observed in the shape of N_2 adsorption and desorption isotherms of ZSC-24 before and after the water vapor treatment, implying that its ordered mesostructure is well retained. Furthermore, the pore size and pore volume are almost unchanged at 7.5 nm and 0.84 cm^3/g, while steaming under the same condition, the ordered mesostructure of SBA-15 was partially collapsed just after 4 h, reducing the pore size from 6.4 to 4.6 nm and the pore volume from 1.06 to 0.43 cm^3/g, a loss of ca. 60 % [24]. This remarkable hydrothermal stability makes such ZSC composites distinct from other composites synthesized at mild temperatures whose pore size and volume experienced a prominent decrease even with treatment at less severe conditions [15, 20]. The preservation of mesoporosity is of important significance since the modern FCC process tends to work with very short contact time (<2 s) [36] where the preservation of large pores benefits mass transfer, and finally improving catalytic performance.

The high hydrothermal stability of nanocrystalline ZSM-5 phase certainly originates from the crystalline framework made up of SiO_4 and AlO_4 units. For the mesoporous phase in the composites, its remarkable hydrothermal stability might be related to the retention of zeolite building units and the high degree of silica condensation in the mesoporous walls as shown by FT-IR and ^{29}Si MAS NMR spectroscopic analyses, respectively, which is in line with the previous studies [24, 30].

Catalytic cracking of cumene and 1,3,5-tri-isopropyl benzene

The catalytic properties of ZSC materials compared to Al-SBA-15 and H-ZSM-5 were investigated in the gas phase cracking of cumene and TIPB as probe reactions. Cumene

Table 4 Cumene and TIPB conversions over various catalysts relative to their acidic properties

Sample	Total acidity[c]	Strong BS[d]	Cumene conversion[e] (%)	TIPB conversion[e] (%)
ZSC-6	0.26	n.a	28.1	78.3
ZSC-12	0.27	0.49	31.2	80.9
ZSC-24	0.34	0.66	80.4	82.5
ZSC-36	0.31	0.80	86.3	40.6
Al-SBA-15[a]	0.18	0.30	13.2	85.2
H-ZSM-5[b]	1.24	5.73	94.4	61.9

Reaction conditions: $T = 300$ °C, WHSV = 1.5 h^{-1}(cumene) or 1 h^{-1} (TIPB), ambient pressure

[a] Synthesized by the same procedure as ZSC, but using the conventional silica-based source instead of zeolite seeds

[b] Commercial Al-rich H-ZSM-5 (Zeocat PZ-2/25)

[c] NH_3-TPD (mmol NH_3/g)

[d] Strong BS are defined as the normalized integral band intensities of pyridine adsorbed on BS (1542 cm^{-1}) after evacuation at 400 °C ($\times 10^{-3}$ a.u.)

[e] Cumene and TIPB conversions after 1 h time-on-stream

cracking is a well-established test reaction to assess strong BS. With a molecular cross-section of 0.5 nm, cumene can enter the pores of ZSM-5 where most strong BS are located. On the contrary, TIPB having three isopropyl units can be easily catalyzed by even weak BS. In addition, with a molecular cross-section of 0.74 nm, TIPB cannot penetrate the pores of ZSM-5 (<0.56 nm), but can diffuse freely in mesopores (ca. 7.4–9.0 nm). By employing them as model compounds, therefore, it is possible to evaluate the effect of the acidic properties and pore sizes of the catalysts on their catalytic performance.

The gas phase cracking of cumene and TIPB were carried out at 300 °C and ambient pressure. Under the tested conditions, the effect of thermal cracking was ruled out as confirmed by no detected conversion of cumene and TIPB over inert material (quartz beads). With the presence of catalysts in this study, cumene and TIPB are mainly dealkylated on BS to yield benzene and di-isopropylbenzene as major products, respectively. This observation indicates that BS are at play in these reactions [6, 18, 37, 38]. The cracking activity over ZSC composites compared to Al-SBA-15 and H-ZSM-5 in the cracking of cumene and TIPB with time-on-stream are presented in Fig. S3 (Supplementary material). The cumene and TIPB conversions after 1 h on-stream are summarized in Table 4.

It is apparent that the cumene conversion heavily depends on strong BS. The cumene conversion over ZSC-36 is higher than over ZSC-24 though the latter sample contains a higher density of acid sites, in particular BS. This means that strong BS are active for cumene cracking rather than weak BS. H-ZSM-5 exhibits the highest cumene conversion (ca. 94 %) as result of the highest concentration of strong BS. ZSC-24 and ZSC-36 display ca. 80 and 86 % cumene conversion, respectively, being comparable to that of H-ZSM-5. Considering the significant difference in the strong BS density of these samples (Table 4) and a lower heat adsorption of cumene on the mesoporous phase with zeolite building units compared to crystalline H-ZSM-5 [9], these results imply that the presence of the mesoporous phase in ZSC composites enhances the access to the active sites of nano-ZSM-5 domains, thereby improving the cumene conversion over ZSC materials even though they have significantly lower densities of strong BS. Similar results have been reported by Waller [8] and others [9, 18]. They found that the dispersion of nano-zeolites in a mesoporous matrix offers a high accessibility to almost all zeolite domains. In contrast, not-dispersed nano-zeolites form aggregates like in case of H-ZSM-5 reducing the accessibility to zeolite domains buried inside the aggregates. ZSC-6 and ZSC-12 with the predominant mesoporous SBA-15 analogs show a mild conversion of around 30 %, which further supports the work of Frunz et al. [9] who found that the high cumene cracking activity of zeolites cannot be attainable with X-ray amorphous zeolite precursors incorporated in the mesoporous walls. However, it should be noted that ZSC-6 and ZSC-12 are still far more active than Al-SBA-15 (13 % cumene conversion). The lowest activity for Al-SBA-15 might be due to the least strong BS caused by its amorphous nature. No obvious relationships between the cumene cracking activity and LS acidity further confirm the crucial role of strong BS in cumene cracking.

In contrast to the cracking of cumene that often serves to evaluate strong BS, the cracking of TIPB allows to test the influence of pore sizes on the catalytic performance. From Table 4, one can see that Al-SBA-15 is the most active catalyst in the cracking of TIPB though it has the lowest cumene conversion. The reason is that TIPB can be easily activated by even weak BS and it has the free access to the active sites inside the mesopores. Compared to Al-SBA-15, ZSC composites with the detectable mesoporous phase (ZSC-6, ZSC-12, and ZSC-24) exhibit slightly lower TIPB conversions of ca. 80 %. This is because TIPB cracking over zeolite phase has proven to occur solely on the external surface with less active sites [6, 14]. However, it appears that the TIPB conversion over ZSC-24 is higher than ZSC-6 and ZSC-12 though the differences are small. This might be due to the occurrence of the interaction at the surface of microporous and mesoporous phases, giving rise to an increase of accessible acid sites [8]. Nevertheless, ZSC-36 containing hardly any mesoporous SBA-15 analogs still affords ca. 40 % TIPB conversion, suggesting that nano-ZSM-5 domains of this sample are quite effective for bulky reactions. Similarly, H-ZSM-5 with very high BS

density and consisting of small crystals displays a fairly high TIPB conversion of 62 % after 1 h on-stream. It has been reported that the TIPB diffusivity and conversion increased greatly as reducing the crystal size of ZSM-5 [6, 9]. Taking it into consideration, such ZSC composites are apparently more active in conversion of bulk hydrocarbons like TIPB compared to other microsized zeolite-based composites [18, 21]. Interestingly, ZSC-24 shows high activity in both cracking of cumene and cracking of TIPB, reaching ca. 80 and 82 % conversion, respectively. These results indicate that the combination of the advantages of nanosized-ZSM-5 (strong BS with high accessibility and shorter diffusion path length) and mesoporous SBA-15 analogs with zeolite building units (increased BS acidity and large pores) leads to the increased density of accessible BS and improved molecular transport, and finally the superior catalytic activity for ZSC-24 in the named reactions.

Conclusions

We presented a synthesis approach for micro-/mesoporous composites that consist of nano-ZSM-5 domains (40–50 nm in diameters) embedded in highly condensed, ordered mesoporous SBA-15 analogs containing zeolite building units. The distribution of microporous and mesoporous phases and the consequent acidic properties can be tuned synthetically by varying the precrystallization time. The bimodal micro-/mesoporous structure is well preserved even upon steaming at 800 °C confirming the remarkable hydrothermal stability of the ZSC composites. The gas phase cracking of cumene and TIPB as probe reactions reveal that the enhanced density of Brønsted acid sites with high accessibility has been achieved over the ZSC composites, giving high conversions of both cumene and TIPB. It is expected that the use of such ZSC composites for the formulation of FCC catalysts or additives lead to an improved performance in the catalytic cracking of heavy oils or biofeeds.

Acknowledgements The authors would like to thank Dr. M.-M. Pohl for recording TEM images, Dr. M. Schneider for XRD measurements, Mr. R. Eckelt for N_2 adsorption and desorption studies; Dr. D.-L. Hoang and Dr. N. Steinfeldt are acknowledged for their help to carry out NH_3-TPD and WAXS/SAXS measurements, respectively. X.-H Vu would like to thank VIED and LIKAT for financial support.

References

1. Corma A (1997) From microporous to mesoporous molecular sieve materials and their use in catalysis. Chem Rev 97: 2373–2419
2. Pérez-Ramírez J, Christensen CH, Egeblad K, Christensen CH, Groen JC (2008) Hierarchical zeolites: enhanced utilisation of microporous crystals in catalysis by advances in materials design. Chem Soc Rev 37:2530–2542
3. Tao Y, Kanoh H, Abrams L, Kaneko K (2006) Mesopore-modified zeolites: preparation, characterization, and applications. Chem Rev 106:896–910
4. Mintova S, Gilson JP, Valtchev V (2013) Advances in nanosized zeolites. Nanoscale 5:6693–6703
5. Viswanadham N, Kamble R, Singh M, Kumar M, Murali Dhar G (2009) Catalytic properties of nano-sized ZSM-5 aggregates. Catal Today 141:182–186
6. Morales-Pacheco P, Domínguez JM, Bucio L, Alvarez F, Sedran U, Falco M (2011) Synthesis of FAU(Y)- and MFI(ZSM5)-nanosized crystallites for catalytic cracking of 1,3,5-triisopropylbenzene. Catal Today 166:25–38
7. Serrano DP, Aguado J, Morales G, Rodríguez JM, Peral A, Thommes M, Epping JD, Chmelka BF (2009) Molecular and meso- and macroscopic properties of hierarchical nanocrystalline ZSM-5 zeolite prepared by seed silanization. Chem Mater 21:641–654
8. Waller P, Shan Z, Marchese L, Tartaglione G, Zhou W, Jansen JC, Maschmeyer T (2004) Zeolite nanocrystals inside mesoporous TUD-1: a high-performance catalytic composite. Chem Eur J 10:4970–4976
9. Frunz L, Prins R, Pirngruber GD (2006) ZSM-5 precursors assembled to a mesoporous structure and its subsequent transformation into a zeolitic phase-from low to high catalytic activity. Micropor Mesopor Mater 88:152–162
10. Landau MV, Tavor D, Regev O, Kaliya ML, Herskowitz M, Valtchev V, Mintova S (1999) Colloidal nanocrystals of zeolite β stabilized in alumina matrix. Chem Mater 11:2030–2037
11. Beck JS, Vartuli JC, Roth WJ, Leonowicz ME, Kresge CT, Schmitt KD, Chu CTW, Olson DH, Sheppard EW, McCullen SB, Higgins JB, Schlenker JL (1992) A new family of mesoporous molecular sieves prepared with liquid crystal templates. J Am Chem Soc 114:10834–10843
12. Zhao D, Feng J, Huo Q, Melosh N, Fredrickson GH, Chmelka BF, Stucky GD (1998) Triblock copolymer syntheses of mesoporous silica with periodic 50 to 300 Angstrom pores. Science 279:548–552
13. Liu Y, Pinnavaia TJ (2002) Aluminosilicate mesostructures with improved acidity and hydrothermal stability. J Mater Chem 12:3179–3190
14. Čejka J, Mintova S (2007) Perspectives of micro/mesoporous composites in catalysis. Catal Rev Sci Eng 49:457–509
15. Liu Y, Zhang W, Pinnavaia TJ (2001) Steam stable MSU-S aluminosilicate mesostructures assembled from zeolite ZSM-5 and zeolite beta seeds. Angew Chem 113:1295–1298
16. Han Y, Wu S, Sun Y, Li D, Xiao FS, Liu J, Zhang X (2002) Hydrothermally stable ordered hexagonal mesoporous aluminosilicates assembled from a triblock copolymer and preformed aluminosilicate precursors in strongly acidic media. Chem Mater 14:1144–1148
17. Gu FN, Wei F, Yang JY, Lin N, Lin WG, Wang Y, Zhu JH (2010) New strategy to synthesis of hierarchical mesoporous zeolites. Chem Mater 22:2442–2450
18. Bagshaw SA, Baxter NI, Brew DRM, Hosie CF, Yuntong N, Jaenicke S, Khuan CG (2006) Highly ordered mesoporous MSU-S_{BEA}/zeolite beta composite material. J Mater Chem 16:2235–2244
19. Wang J, Groen JC, Yue W, Zhou W, Coppens MO (2008) Facile synthesis of ZSM-5 composites with hierarchical porosity. J Mater Chem 18:468–474
20. Xia Y, Mokaya R (2004) On the synthesis and characterization of ZSM-5/MCM-48 aluminosilicate composite materials. J Mater Chem 14:863–870

21. Xia Y, Mokaya R (2004) Are mesoporous silicas and aluminosilicas assembled from zeolite seeds inherently hydrothermally stable? Comparative evaluation of MCM-48 materials assembled from zeolite seeds. J Mater Chem 14:3427–3435
22. Liu L, Xiong G, Wang X, Cai J, Zhao Z (2009) Direct synthesis of disordered micro–mesoporous molecular sieve. Micropor Mesopor Mater 123:221–227
23. Lee DS, Liu TK (2001) Synthesis of micropore/mesopore composite materials. React Kinet Catal Lett 72:209–218
24. Vu XH, Steinfeldt N, Armbruster U, Martin A (2012) Improved hydrothermal stability and acidic properties of ordered mesoporous SBA-15 analogs assembled from nanosized ZSM-5 precursors. Micropor Mesopor Mater 164:120–126
25. Tokay B, Somer M, Erdem-Şenatalar A, Schüth F, Thompson RW (2009) Nanoparticle silicalite-1 crystallization from clear solutions: nucleation. Micropor Mesopor Mater 118:143–151
26. Petkov N, Hölzl M, Metzger TH, Mintova S, Bein T (2005) Ordered micro/mesoporous composite prepared as thin films. J Phys Chem B 109:4485–4491
27. Huang L, Guo W, Deng P, Xue Z, Li Q (2000) Investigation of synthesizing MCM-41/ZSM-5 composites. J Phys Chem B 104:2817–2823
28. Jacobsen CJH, Madsen C, Janssens TVW, Jakobsen HJ, Skibsted J (2000) Zeolites by confined space synthesis-characterization of the acid sites in nanosized ZSM-5 by ammonia desorption and ^{27}Al/^{29}Si-MAS NMR spectroscopy. Micropor Mesopor Mater 39:393–401
29. Guo W, Xiong C, Huang L, Li Q (2001) Synthesis and characterization of composite molecular sieves comprising zeolite beta with MCM-41 structures. J Mater Chem 11:1886–1890
30. Pan D, Yuan P, Zhao L, Liu N, Zhou L, Wei G, Zhang J, Ling Y, Fan Y, Wei B, Liu H, Yu C, Bao X (2009) New understanding and simple approach to synthesize highly hydrothermally stable and ordered mesoporous materials. Chem Mater 21:5413–5425
31. Xue Z, Zhang T, Ma J, Miao H, Fan W, Zhang Y, Li R (2012) Accessibility and catalysis of acidic sites in hierarchical ZSM-5 prepared by silanization. Micropor Mesopor Mater 151:271–276
32. Serrano DP, García RA, Vicente G, Linares M, Procházková D, Čejka J (2011) Acidic and catalytic properties of hierarchical zeolites and hybrid ordered mesoporous materials assembled from MFI protozeolitic units. J Catal 279:366–380
33. Luan Z, Fournier JA (2005) In situ FTIR spectroscopic investigation of active sites and adsorbate interactions in mesoporous aluminosilicate SBA-15 molecular sieves. Micropor Mesopor Mater 79:235–240
34. Crepeau G, Montouillout V, Vimont A, Mariey L, Cseri T, Mauge F (2006) Nature, structure and strength of the acidic sites of amorphous silica alumina: an IR and NMR study. J Phys Chem B 110:15172–15185
35. Chen YM (2006) Recent advances in FCC technology. Powder Technol 163:2–8
36. Harding RH, Peters AW, Nee JRD (2001) New developments in FCC catalyst technology. Appl Catal A 221:389–396
37. Corma A, Wojciechowski BW (1982) The catalytic cracking of cumene. Catal Rev Sci Eng 24:1–65
38. Kumaran GM, Garg S, Soni K, Kumar M, Gupta JK, Sharma LD, Rao KSR, Dhar GM (2008) Synthesis and characterization of acidic properties of Al-SBA-15 materials with varying Si/Al ratios. Micropor Mesopor Mater 114:103–109